Quantitative characterization of the spin-orbit torque using harmonic Hall voltage measurements

Masamitsu Hayashi,[1,*] Junyeon Kim,[1] Michihiko Yamanouchi,[2,3] and Hideo Ohno[2,3,4]
[1]*National Institute for Materials Science, Tsukuba 305-0047, Japan*
[2]*Center for Spintronics Integrated Systems, Tohoku University, Sendai 980-8577, Japan*
[3]*Research Institute of Electrical Communication, Tohoku University, Sendai 980-8577, Japan*
[4]*WPI Advanced Institute for Materials Research, Tohoku University, Sendai 980-8577, Japan*
(Received 10 October 2013; revised manuscript received 5 March 2014; published 29 April 2014)

Solid understanding of current induced torques is a key to the development of current and voltage controlled magnetization dynamics in ultrathin magnetic heterostructures. To evaluate the size and direction of such torques, or effective fields, a number of methods have been employed. Here, we examine the adiabatic (low-frequency) harmonic Hall voltage measurement that has been used to study the effective field. We derive an analytical formula for the harmonic Hall voltages to evaluate the effective field for both out of plane and in-plane magnetized systems. The formula agrees with numerical calculations based on a macrospin model. Two different in-plane magnetized films, Pt|CoFeB|MgO and CuIr|CoFeB|MgO are studied using the formula developed. The effective field obtained for the latter system shows relatively good agreement with that estimated using spin torque switching phase diagram measurements reported previously. Our results illustrate the versatile applicability of harmonic Hall voltage measurement for studying current induced torques in magnetic heterostructures.

DOI: 10.1103/PhysRevB.89.144425 PACS number(s): 85.75.−d, 72.25.Hg, 75.70.Tj, 75.76.+j

I. INTRODUCTION

Application of current to systems with large spin-orbit coupling in bulk or at interfaces may result in spin current generation and/or spin accumulation via the spin Hall effect [1–3] or the Rashba-Edelstein effect [4,5]. When spin current is generated in neighboring nonmagnetic (NM) layer(s) via the spin Hall effect, such spin current can diffuse into the ferromagnetic (FM) layer and exert torque on the moments via spin transfer torque [6,7]. Alternatively, spin accumulation can take place at the NM|FM interface via the Rashba-Edelstein effect (i.e., current induced spin polarization). Accumulated spins at the interface can force the moments to change its direction by direct exchange coupling [8,9]. These effects are referred to as the "spin-orbit torques" [9–15], which is to be distinguished from conventional spin transfer torque since the spin-orbit coupling plays a critical role in generating spin current and spin accumulation.

Spin-orbit torques are attracting great interest as they can lead to magnetization switching in geometries which were not possible with conventional spin transfer torque [16,17] and unprecedented fast domain wall motion [18,19]. Solid understanding of how these torques arise is thus essential for developing devices utilizing spin-orbit effects in ultrathin magnetic heterostructures.

Recently, it has been reported that an adiabatic (low-frequency) harmonic Hall voltage measurement, originally developed by Pi *et al.* [20], can be used to evaluate the "effective magnetic field" [20–22] that generates the torque acting on the magnetic moments [23–25]. This technique has been used to evaluate the size and direction of the effective field in magnetic heterostructures. Using such technique, we have previously shown that the effective field shows a strong dependence on the thickness of Ta and CoFeB layers in Ta|CoFeB|MgO heterostructures [23]. The difference in the sign of the spin Hall angle between Ta and Pt has been probed and reported recently [25]. It has also been shown that there is a strong angular dependence (the angle between the magnetization and the current flow direction) of the effective field in various heterostructures [24]. Nonlocal effects, i.e., spin current generated in a Pt layer can propagate through a Cu spacer and exert torques on the magnetic layer, have been probed using a similar technique [26]. These results show that the adiabatic harmonic Hall voltage measurement is a useful tool to study spin-orbit torques in ultrathin magnetic heterostructures.

The effective fields evaluated using different techniques vary, in some cases, by orders of magnitude [17,20–22]. It is thus important to examine the accuracy of the characterization method used. With regard to the adiabatic harmonic Hall measurements, its application to in-plane magnetized systems has been limited, primarily due to the difficulty in obtaining one of the two components (i.e., the dampinglike term) of the effective field. To address these issues, here we derive an analytical formula that describes the harmonic Hall voltages and compare it to numerical calculations based on a macrospin model to test its validity. We extend our approach, which was previously limited to evaluate out-of-plane magnetized samples, to characterize in-plane magnetized systems. The formula developed is applied to two different in-plane magnetized systems, Pt|CoFeB|MgO and CuIr|CoFeB|MgO. The effective field obtained for the latter system agrees with that estimated using spin torque switching phase diagrams [27].

II. ANALYTICAL SOLUTIONS

A. Modulation amplitude of the magnetization angle

When current is passed to the device under test, current induced effective field $\Delta H_{X,Y,Z}$, including the Oersted field, can modify the magnetization angle from its equilibrium value (θ_0, φ_0). This section describes how this current induced modulation of the magnetization angle, termed the modulation amplitudes ($\Delta\theta, \Delta\varphi$) hereafter, is analytically derived. The final results are given in Eqs. (14) and (15).

The magnetic energy of the system can be expressed as

$$E = -K_{EFF}\cos^2\theta - K_I \sin^2\varphi \sin^2\theta - \vec{M}\cdot\vec{H}, \qquad (1)$$

*hayashi.masamitsu@nims.go.jp

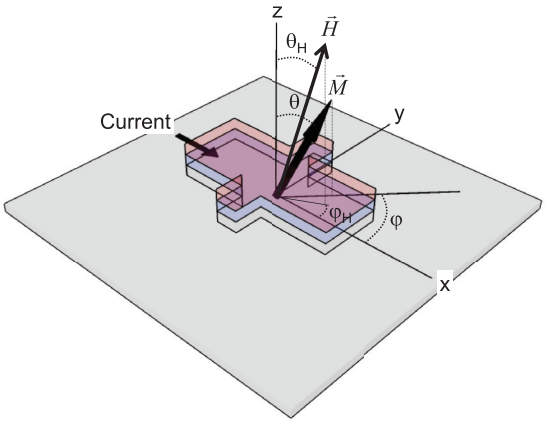

FIG. 1. (Color online) Schematic illustration of the experimental setup. A Hall bar is patterned from a magnetic heterostructure consisting of a nonmagnetic metal layer (gray), a ferromagnetic metal layer (blue), and an insulating oxide layer (red). The large gray square is the substrate with an insulating oxide surface. Definitions of the coordinate systems are illustrated together. $\vec{M}$ denotes the magnetization and $\vec{H}$ represents the external field.

where θ and φ are the polar and azimuthal angles, respectively, of the magnetization $\vec{M}$ (see Fig. 1 for the definition), defined as

$$\vec{M} = M_S\hat{m}, \hat{m} = (\sin\theta\cos\varphi, \sin\theta\sin\varphi, \cos\theta), \tag{2}$$

M_s is the saturation magnetization, $\hat{m}$ is a unit vector representing the magnetization direction. The direction of the external magnetic field $\vec{H}$ is expressed using its polar and azimuthal angles (θ_H, φ_H) as

$$\vec{H} = H(\sin\theta_H\cos\varphi_H, \sin\theta_H\sin\varphi_H, \cos\theta_H). \tag{3}$$

K_{EFF} is the effective out of plane anisotropy energy and K_I is the in-plane easy axis anisotropy energy. K_{EFF} and K_I can be expressed as the following using the demagnetization coefficients N_i ($\sum_{i=X,Y,Z} N_i = 4\pi$) and the uniaxial magnetic anisotropy energy K_U:

$$K_{EFF} = K_U - \tfrac{1}{2}(N_Z - N_X)M_S^2,$$
$$K_I = \tfrac{1}{2}(N_X - N_Y)M_S^2. \tag{4}$$

K_U is defined positive for out of plane magnetic easy axis. We use the convention of polar coordinates ($0 \leqslant \theta_H \leqslant \pi$ and $0 \leqslant \varphi_H \leqslant 2\pi$) here.

The equilibrium magnetization direction (θ_0, φ_0) is calculated using the following two equations:

$$\frac{\partial E}{\partial\theta} = 0 = (K_{EFF} - K_I\sin^2\varphi_0)\sin 2\theta_0 - M_S H[\cos\theta_0\sin\theta_H(\cos\varphi_0\cos\varphi_H + \sin\varphi_0\sin\varphi_H) - \sin\theta_0\cos\theta_H], \tag{5}$$

$$\frac{\partial E}{\partial\varphi} = 0 = -K_I\sin^2\theta_0\sin 2\varphi_0 - M_S H\sin\theta_0\sin\theta_H\sin(\varphi_H - \varphi_0). \tag{6}$$

Equations (5) and (6) can be solved to obtain (θ_0, φ_0). To simplify notations, we define

$$H_K \equiv \frac{2K_{EFF}}{M_S}, \quad H_A \equiv \frac{2K_I}{M_S}. \tag{7}$$

The modulation amplitudes $(\Delta\theta, \Delta\varphi)$, i.e., the change in the magnetization angle from its equilibrium value (θ_0, φ_0) due to the effect of current induced effective field $\Delta\vec{H}$, are given by [24,28]

$$\Delta\theta = \frac{\partial\theta}{\partial H_X}\Delta H_X + \frac{\partial\theta}{\partial H_Y}\Delta H_Y + \frac{\partial\theta}{\partial H_Z}\Delta H_Z, \tag{8}$$

$$\Delta\varphi = \frac{\partial\varphi}{\partial H_X}\Delta H_X + \frac{\partial\varphi}{\partial H_Y}\Delta H_Y + \frac{\partial\varphi}{\partial H_Z}\Delta H_Z. \tag{9}$$

Here, $\frac{\partial\theta}{\partial H_i}$ and $\frac{\partial\varphi}{\partial H_i}$ represent the degree of change in the angles when ΔH_i is applied. Throughout this paper, subscript i denotes the $i(=X,Y,Z)$ component of the corresponding vector. (ΔH_i does not necessarily have to be current related fields, but here it is understood as the current induced fields including those due to spin-orbit torques and the Oersted field.)

To calculate $\frac{\partial\theta}{\partial H_i}$ and $\frac{\partial\varphi}{\partial H_i}$, we use the following relations derived from Eqs. (5) and (6):

$$\frac{\partial}{\partial H_i}\left(\frac{\partial E}{\partial\theta}\right) = 0 = [(K_{EFF} - K_I\sin^2\varphi_0)2\cos 2\theta_0 - M_S(-H_X\sin\theta_0\cos\varphi_0 - H_Y\sin\theta_0\sin\varphi_0 - H_Z\cos\theta_0)]\frac{\partial\theta}{\partial H_i} + [-K_I\sin 2\theta_0\sin 2\varphi_0 - M_S\cos\theta_0(-H_X\sin\varphi_0 + H_Y\cos\varphi_0)]\frac{\partial\varphi}{\partial H_i} - M_S f_i, \tag{10}$$

$$\frac{\partial}{\partial H_i}\left(\frac{\partial E}{\partial\varphi}\right) = 0 = [-K_I\cos\theta_0\sin 2\varphi_0 + M_S\cos\theta_0(H_X\sin\varphi_0 - H_Y\cos\varphi_0)]\frac{\partial\theta}{\partial H_i} + [-2K_I\sin\theta_0\cos 2\varphi_0 + M_S\sin\theta_0(H_X\cos\varphi_0 + H_Y\sin\varphi_0)]\frac{\partial\varphi}{\partial H_i} + M_S g_i, \tag{11}$$

where

$$\vec{f} = [\cos\theta_0\cos\varphi_0, \cos\theta_0\sin\varphi_0, -\sin\theta_0], \quad \vec{g} = [\sin\theta_0\sin\varphi_0, -\sin\theta_0\cos\varphi_0, 0].$$

The coupled equations (10) and (11) can be solved for $\frac{\partial\theta}{\partial H_i}$ and $\frac{\partial\varphi}{\partial H_i}$, which reads

$$\frac{\partial\theta}{\partial H_i} = \frac{1}{F_1}(f_i - Cg_i), \tag{12}$$

$$\frac{\partial\varphi}{\partial H_i} = \frac{1}{F_1 F_2}\left\{ f_i\left[\frac{1}{2}H_A \sin 2\theta_0 \sin 2\varphi_0 - \cos\theta_0 (H_X \sin\varphi_0 - H_Y \cos\varphi_0)\right] - g_i\left[(H_K - H_A \sin^2\varphi_0)\cos 2\theta_0 + \vec{H}\cdot\hat{m}\right]\right\}, \quad (13)$$

$$F_1 \equiv (H_K - H_A \sin^2\varphi_0)\cos 2\theta_0 + \vec{H}\cdot\hat{m} - C\left[\frac{1}{2}H_A \sin 2\theta_0 \sin 2\varphi_0 - \cos\theta_0 (H_X \sin\varphi_0 - H_Y \cos\varphi_0)\right],$$

$$F_2 \equiv -H_A \sin^2\theta_0 \cos 2\varphi_0 + (H_X \cos\varphi_0 + H_Y \sin\varphi_0)\sin\theta_0,$$

$$C \equiv \frac{1}{F_2}\left[\frac{1}{2}H_A \sin 2\theta_0 \sin 2\varphi_0 - \cos\theta_0 (H_X \sin\varphi_0 - H_Y \cos\varphi_0)\right].$$

To obtain a simplified expression for $\Delta\theta$ and $\Delta\varphi$, we make the following assumptions that are usually satisfied in the experiments. First, we consider $|H_A| \ll |H\sin\theta_H|$, a requirement which is, in general, met since in-plane magnetic anisotropy is small for many material systems. (Since H_A includes shape anisotropy, high aspect ratio nanowires may not satisfy this condition.) Assuming $|H_A| \ll |H\sin\theta_H|$ in Eq. (6) gives $\varphi_0 = \varphi_H$, which simplifies many expressions. Next, we assume that the in-plane component of the external field H is directed along (or close to) one of the Cartesian coordinate axes (along x or y axis). Fixing the external field (and thus the magnetization direction because of the previous assumption) along one of the high-symmetry axes considerably simplifies many of the expressions (see Appendix for the details).

With these assumptions and substitution of Eqs. (12) and (13) into Eqs. (8) and (9), we obtain the following expressions for the modulation amplitudes of the magnetization angle (for φ_H along the x and y axes):

$$\Delta\theta = \frac{\cos\theta_0 (\Delta H_X \cos\varphi_H + \Delta H_Y \sin\varphi_H) - \sin\theta_0 \Delta H_Z}{(H_K - H_A \sin^2\varphi_H)\cos 2\theta_0 + H\cos(\theta_H - \theta_0)}, \quad (14)$$

$$\Delta\varphi = \frac{-\Delta H_X \sin\varphi_H + \Delta H_Y \cos\varphi_H}{-H_A \sin\theta_0 \cos 2\varphi_H + H\sin\theta_H}. \quad (15)$$

B. Expression for the Hall voltage

The Hall voltage typically contains contributions from the anomalous Hall effect (AHE) and the planar Hall effect (PHE) [24,29,30]. We define ΔR_A and ΔR_P as the change in the Hall resistance due to the AHE and PHE, respectively. Assuming a current flow along the x axis, which is different from the convention used in our previous report [23], the Hall resistance R_{XY} is expressed as

$$R_{XY} = \tfrac{1}{2}\Delta R_A \cos\theta + \tfrac{1}{2}\Delta R_P \sin^2\theta \sin 2\varphi. \quad (16)$$

Note that contribution from the ordinary Hall effect, which are neglected here, can influence the measurement depending on the material and the measurement condition. If we substitute $\theta = \theta_0 + \Delta\theta, \varphi = \varphi_0 + \Delta\varphi$ and assume $\Delta\theta \ll 1$ and $\Delta\varphi \ll 1$, Eq. (16) can be expanded to read

$$\begin{aligned} R_{XY} \approx{}& \tfrac{1}{2}\Delta R_A (\cos\theta_0 - \Delta\theta \sin\theta_0) \\ &+ \tfrac{1}{2}\Delta R_P(\sin^2\theta_0 + \Delta\theta \sin 2\theta_0)(\sin 2\varphi_0 \\ &+ 2\Delta\varphi \cos 2\varphi_0). \end{aligned} \quad (17)$$

The Hall voltage V_{XY} is a product of the Hall resistance R_{XY} and the current I passed along the device, i.e.,

$$V_{XY} = R_{XY} I. \quad (18)$$

When a sinusoidal current ($I = \Delta I \sin\omega t$) is applied, the current induced effective field oscillates in sync with the current. Note that the frequency of the oscillating current ω is small enough (typically in the hertz range) so that the phase difference, if any, between the current and the effective field oscillations can be ignored. Thus ΔH_i in Eqs. (14) and (15) need to be replaced with $\Delta H_i \sin\omega t$ to accommodate the oscillating effective field. This results in replacing $\Delta\theta$ and $\Delta\varphi$ in Eq. (17) with $\Delta\theta \sin\omega t$ and $\Delta\varphi \sin\omega t$, respectively. Substituting the modified Eq. (17) into Eq. (18) give

$$\begin{aligned} V_{XY} &= V_0 + V_\omega \sin\omega t + V_{2\omega}\cos 2\omega t, \\ V_0 &= \tfrac{1}{2}(B_\theta + B_\varphi)\Delta I, \\ V_\omega &= A\Delta I, \\ V_{2\omega} &= -\tfrac{1}{2}(B_\theta + B_\varphi)\Delta I, \\ A &= \tfrac{1}{2}\Delta R_A \cos\theta_0 + \tfrac{1}{2}\Delta R_P \sin^2\theta_0 \sin 2\varphi_0, \\ B_\theta &= \tfrac{1}{2}(-\Delta R_A \sin\theta_0 + \Delta R_P \sin 2\theta_0 \sin 2\varphi_0)\Delta\theta, \\ B_\varphi &= \Delta R_P \sin^2\theta_0 \cos 2\varphi_0 \Delta\varphi. \end{aligned} \quad (19)$$

As evident in Eq. (19), the second harmonic Hall voltage $V_{2\omega}$ contains information of ΔH_i through $\Delta\theta$ and $\Delta\varphi$ [Eqs. (14) and (15)]. Note that Eq. (19) describes the harmonic Hall voltage in the limit of small $\Delta\theta$ and $\Delta\varphi$.

C. Relation between the current induced effective field and spin torque

To illustrate the relationship between the current induced effective field ΔH_i and the conventional spin torque terms, ΔH_i can be added, in the form of vector $\Delta\vec{H}$, in the Landau-Lifshitz-Gilbert (LLG) equation:

$$\frac{\partial\hat{m}}{\partial t} = -\gamma\hat{m}\times\left(-\frac{\partial E}{\partial\vec{M}} + \Delta\vec{H}\right) + \alpha\hat{m}\times\frac{\partial\hat{m}}{\partial t}. \quad (20)$$

Here, α is the Gilbert damping constant, γ is the gyromagnetic ratio, $-\frac{\partial E}{\partial\vec{M}}$ is the current independent effective magnetic fields that include external, exchange, anisotropy and demagnetization fields. Equation (20) can be compared to the general LLG equation that includes the two spin torque terms:

$$\frac{\partial\hat{m}}{\partial t} = -\gamma\hat{m}\times\left(-\frac{\partial E}{\partial\vec{M}} + a_J(\hat{m}\times\hat{p}) + b_J\hat{p}\right) + \alpha\hat{m}\times\frac{\partial\hat{m}}{\partial t}. \quad (21)$$

Here, $\hat{p}$ represents the magnetization direction of the "reference layer" in spin valve nanopillars/magnetic tunnel

junctions, a_J and b_J correspond to the dampinglike (Slonczweski-Berger) term [6,7] and the fieldlike term [31], respectively. In magnetic heterostructures where spin-orbit torques need to be considered, $\hat{p}$ represents the average spin direction of the electrons diffusing into the magnetic layer. Comparing Eqs. (20) and (21), we can decompose the current induced effective field $\Delta\vec{H}$ into two terms, the dampinglike term $a_J\hat{m}\times\hat{p}$ and the fieldlike term $b_J\hat{p}$. The dampinglike term depends on the magnetization direction whereas the fieldlike term is independent of $\hat{m}$. Thus one can identify whether the effective field is dampinglike or fieldlike by measuring its dependence on the magnetization direction.

In general, a_J and b_J are not constant and depend on the relative angle between $\hat{m}$ and $\hat{p}$. For example, a_J depends [32,33] on $\hat{m}\cdot\hat{p}$, which manifests itself in the magnetization angular dependence of giant magnetoresistance [34] and spin torque induced effects [35]. Recently, it has been reported that both a_J and b_J show significant dependence on the angle of magnetization in ultrathin magnetic heterostructures [24]. Here we assume that a_J and b_J are constant for simplicity. This is because the magnetization angle does not vary much during the experiments for the majority of our approaches described here. The only exception applies to case described in Sec. III B 2 where the effect of the angular dependence of a_J and b_J is briefly discussed.

For the numerical calculations, we use $\hat{p}=(0,1,0)$; this represents, for example, the spin direction of the electrons entering the CoFeB layer via the spin Hall effect in Ta when current is passed along the $+x$ direction in Ta|CoFeB|MgO heterostructures [23]. In the following, we consider two representative cases, systems with out of plane and in-plane magnetizations.

III. APPROXIMATE EXPRESSIONS FOR THE HARMONIC HALL VOLTAGES

A. Out-of-plane magnetization systems

We first consider a system where the magnetization points along the film normal owing to its perpendicular magnetic anisotropy. To obtain analytical solutions for the harmonic Hall voltages, we assume the equilibrium magnetization direction does not deviate much from the z-axis, i.e., $\theta_0=\theta_0'\,(\theta_0'\ll 1)$ for $\vec{M}$ along $+\hat{z}$ and $\theta_0=\pi-\theta_0'\,(\theta_0'\ll 1)$ for $\vec{M}$ along $-\hat{z}$. Keeping terms that are linear with θ_0', Eqs. (5) and (6) give

$$\theta_0'=\frac{H\sin\theta_H}{(H_K-H_A\sin^2\varphi_H)\pm H\cos\theta_H},\quad \varphi_0=\varphi_H. \tag{22}$$

Note that $|H_A|\ll|H\sin\theta_H|$ is assumed in Eq. (6) to obtain $\varphi_0=\varphi_H$. The $\pm$ sign corresponds to the case for $\vec{M}$ pointing along $\pm\hat{z}$. Substituting Eq. (22) into Eqs. (14), (15), and (19) give

$$V_\omega\approx\pm\frac{1}{2}\Delta R_A\left[1-\frac{1}{2}\left(\frac{H\sin\theta_H}{H_K\pm H\cos\theta_H}\right)^2\right]\Delta I, \tag{23}$$

$$\begin{aligned}V_{2\omega}\approx&-\frac{1}{4}[\mp\Delta R_A(\Delta H_X\cos\varphi_H+\Delta H_Y\sin\varphi_H)\\&+2\Delta R_P(-\Delta H_X\sin\varphi_H+\Delta H_Y\cos\varphi_H)\cos 2\varphi_H]\\&\times\frac{H\sin\theta_H}{(H_K\pm H\cos\theta_H)^2}\Delta I.\end{aligned} \tag{24}$$

Equation (24) shows that the planar Hall effect mixes the signal from different components of the current induced effective field [24]. For systems with negligible PHE, ΔH_X (ΔH_Y) can be determined by measuring $V_{2\omega}$ as a function of the external in-plane field directed along the x (y) axis. However, if the PHE becomes comparable to the size of AHE, contribution from the *orthogonal component* appears in $V_{2\omega}$ via the PHE. For example, when ΔR_P is larger than half of ΔR_A, ΔH_Y (ΔH_X) becomes the dominant term in $V_{2\omega}$ for field sweep along the x (y) axis. Thus to estimate the effective field components accurately in systems with non-negligble PHE, one needs to measure $V_{2\omega}$ in two orthogonal directions and analytically calculate each component, as described below.

We follow the procedure used previously [23] to eliminate the prefactors that are functions of ΔI and H_K in Eqs. (23) and (24). $\theta_H=\pi/2$ is substituted in Eqs. (23) and (24) since the external field is swept along the film plane. The respective curvature and slope of V_ω and $V_{2\omega}$ versus the external field are calculated to obtain the ratio B, defined as

$$\begin{aligned}B\equiv&\left(\frac{\partial V_{2\omega}}{\partial H}\Big/\frac{\partial^2 V_\omega}{\partial H^2}\right)\\=&-\frac{1}{2}\left[\left(\Delta H_X\mp 2\frac{\Delta R_P}{\Delta R_A}\cos 2\varphi_H\Delta H_Y\right)\cos\varphi_H\right.\\&\left.+\left(\Delta H_Y\pm 2\frac{\Delta R_P}{\Delta R_A}\cos 2\varphi_H\Delta H_X\right)\sin\varphi_H\right].\end{aligned} \tag{25}$$

We define $B_X\equiv(\frac{\partial V_{2\omega}}{\partial H}/\frac{\partial^2 V_\omega}{\partial H^2})|_{\vec{H}\parallel\hat{x}}$ and $B_Y\equiv(\frac{\partial V_{2\omega}}{\partial H}/\frac{\partial^2 V_\omega}{\partial H^2})|_{\vec{H}\parallel\hat{y}}$, which correspond to B when the external field H is directed along the x and y axes, respectively, and $\xi\equiv\frac{\Delta R_P}{\Delta R_A}$, which is the ratio of the PHE and AHE resistances. Finally, we obtain

$$\begin{aligned}\Delta H_X&=-2\frac{(B_X\pm 2\xi B_Y)}{1-4\xi^2},\\\Delta H_Y&=-2\frac{(B_Y\pm 2\xi B_X)}{1-4\xi^2}.\end{aligned} \tag{26}$$

The $\pm$ sign corresponds to $\vec{M}$ pointing along $\pm\hat{z}$. Equation (26) provides a simple method to obtain the effective field under circumstances where both AHE and PHE contribute to the Hall signal. When PHE is negligible, $\xi=0$ and we recover the form derived previously [23].

B. In-plane magnetization systems

We next consider systems with in-plane magnetization (easy axis is along the x axis). Note that $H_K<0$ for in-plane magnetized systems. Following the previous discussions, the external field must be swept along two directions orthogonal to the magnetization direction to obtain each component of the effective field (the dampinglike and the fieldlike terms). For in-plane magnetized samples, the two directions are: along the film normal and along a direction within the film plane that is transverse to the magnetization direction. From the discussions on the out of plane magnetized samples and considering the symmetry of the system, for in-plane magnetized samples, one may expect to obtain the dampinglike term from the out of plane field sweep and the fieldlike term from the in-plane transverse field sweep. It turns out that [see Eq. (29) and below] the out of plane field sweep gives information of the fieldlike

term whereas the in-plane transverse field sweep provides that of the dampinglike term when $|H_K| \gg |H_A|$, which we consider here. This is due to the larger contribution of the planar Hall effect on the second harmonic signal ($V_{2\omega}$) over that of the anomalous Hall effect. In theory, one can perform both measurements along each field direction to obtain the fieldlike and dampinglike terms. However, for the latter, the assumption $|H_A| \ll |H \sin\theta_H|$ causes the magnetization to rotate along the transverse field direction as soon as $|H|$ is larger than $|H_A|$, thus hindering evaluation of the dampinglike term.

To circumvent this difficulty, we show two alternative approaches. One is to make use of the anisotropic magnetoresistance (AMR) of the magnetic material and measure the longitudinal voltage (V_{XX}), which in turn provides information of the dampinglike term. The external field is swept along the film normal but must be kept small to maintain $\theta_0' \ll 1$ when $\theta_0 = \frac{\pi}{2} \pm \theta_0'$. During the field sweep, one can measure V_{XY} and V_{XX} to obtain the fieldlike and dampinglike terms, respectively. The second approach is to sweep the external field (H) again along the film normal but in a larger field range, i.e., $|H|$ must be larger than the anisotropy field ($|H_K|$). Here, the second harmonic voltage at low field provides information on the fieldlike term, as noted above, but its high field value (when $|H| \sim \pm|H_K|$) gives information on the dampinglike term. We start from the small field limit with simultaneous measurements of Hall and longitudinal voltage measurements, followed by the large field sweep measurements.

1. Low field limit

a. Harmonic Hall voltage and the fieldlike term. The external field is directed along or close to the film normal ($\theta_H \sim 0$ or π) but small enough so that the equilibrium magnetization direction does not deviate much from the film plane, i.e., $\theta_0 = \frac{\pi}{2} + \theta_0' \left(\theta_0' \ll 1\right)$ for $\vec{M}$ pointing along one direction within the film plane and $\theta_0 = \frac{\pi}{2} - \theta_0' \left(\theta_0' \ll 1\right)$ for the case where the direction of $\vec{M}$ is reversed from the former ($\varphi_0 \to \varphi_0 + \pi$). We assume $\varphi_0 \sim \varphi_H$. Keeping terms that are linear with θ_0', Eqs. (5) and (6) give

$$\theta_0' = \pm \frac{H \cos\theta_H}{(H_K - H_A \sin^2\varphi_H) - H \sin\theta_H}, \quad \varphi_0 \sim \varphi_H. \tag{27}$$

The $\pm$ sign corresponds to the case for $\theta_0 = \theta_0' \pm \frac{\pi}{2}$. Substituting Eq. (27) into Eqs. (14), (15) and (19) give

$$V_\omega \approx -\frac{1}{2} \Delta R_A \frac{H \cos\theta_H}{(H_K - H_A \sin^2\varphi_H) - H \sin\theta_H} \Delta I, \tag{28}$$

$$V_{2\omega} \approx -\frac{1}{2}\left[\frac{1}{2}\Delta R_A \frac{\Delta H_Z}{-(H_K - H_A \sin^2\varphi_H) + H \sin\theta_H} + \Delta R_P \frac{(-\Delta H_X \sin\varphi_H + \Delta H_Y \cos\varphi_H)\cos 2\varphi_H}{-H_A \cos 2\varphi_H + H \sin\theta_H}\right] \Delta I. \tag{29}$$

The second term (the ΔR_P term) in Eq. (29) dominates the second harmonic voltage for samples with large $|H_K|$, which is usually the case for in-plane magnetic materials (H_K includes the demagnetization field). Thus, for a typical in-plane magnetized sample, one can ignore the first term in Eq. (29) if the external field is small (i.e., $|H| \ll |H_K|$) and obtain

$$V_{2\omega} \approx -\frac{1}{2}\left[\Delta R_P \frac{(-\Delta H_X \sin\varphi_H + \Delta H_Y \cos\varphi_H)\cos 2\varphi_H}{-H_A \cos 2\varphi_H + H \sin\theta_H}\right] \Delta I. \tag{30}$$

When the magnetization points along the x axis and the incoming electrons' spin polarization is set along the y axis [$\hat{p} = (0, \pm 1, 0)$], the dampinglike *effective field* is directed along the film normal (not to be confused with the dampinglike *torque* that points along the film plane) and its in-plane component ΔH_X is nearly zero. See the inset of Fig. 3(b) in which we show the three effective field components ΔH_i for this geometry. Thus in Eq. (30), only the fieldlike term ΔH_Y remains.

Equation (30) indicates that when the field is exactly along the film normal ($\theta_H = 0$ or π), the field dependence of $V_{2\omega}$ vanishes. Experimentally, it is preferable to look at the *field dependence* of $V_{2\omega}$ rather than its absolute value to obtain ΔH_Y (see, for example, Fig. 5(d) and the related discussion). Thus we apply a tilted magnetic field ($0 < \theta_H < \pi$) in using Eq. (30).

Using Eqs. (28) and (30), we derive a simple formula, similar to that shown in Eq. (25), to estimate ΔH_Y. For a tilted external field, it is preferable to apply the in-plane field component along the magnetic easy axis ($\varphi_H = 0$ or π) to unambiguously set the equilibrium magnetization azimuthal angle φ_0. Substituting $\varphi_H = 0$ in Eqs. (28) and (30) gives

$$\frac{\partial V_\omega}{\partial H} \approx -\frac{1}{2}\Delta R_A \Delta I \frac{\cos\theta_H}{H_K}, \tag{31}$$

$$\frac{\partial (1/V_{2\omega})}{\partial H} \approx -\frac{2\sin\theta_H}{\Delta R_P \Delta I \Delta H_Y}. \tag{32}$$

Thus ΔH_Y (the fieldlike term) can be obtained by

$$\Delta H_Y \approx \frac{\sin 2\theta_H}{2\xi H_K}\left[1 \Big/ \left(\frac{\partial V_\omega}{\partial H}\right)\left(\frac{\partial (1/V_{2\omega})}{\partial H}\right)\right]. \tag{33}$$

Unlike the case derived in the previous section [Eq. (25)], here one needs to substitute H_K and θ_H to calculate the effective field. This is because the field dependence of the first harmonic voltage is primarily determined by the change in the magnetization direction along the z axis (relevant anisotropy is H_K), whereas that of the second harmonic voltage is dominated by the magnetization angular change within the film plane (relevant anisotropy is H_A); therefore taking the ratio of the two harmonic voltages will not cancel out H_K (and θ_H).

b. Harmonic longitudinal voltage and the dampinglike term. As noted above, in order to obtain the dampinglike term, one can make use of the AMR effect, if any, of the magnetic material. The longitudinal resistance R_{XX} is expressed as

$$R_{XX} = R_0 + \tfrac{1}{2}\Delta R_{MR} \sin^2\theta \cos^2\varphi, \tag{34}$$

where R_0 and ΔR_{MR} are, respectively, the resistance independent of the magnetization direction and the change in the resistance due to the AMR effect. The current is assumed to flow along the x axis. We substitute $\theta = \theta_0 + \Delta\theta$, $\varphi = \varphi_0 + \Delta\varphi$ into Eq. (34) and assume $\Delta\theta \ll 1$ and $\Delta\varphi \ll 1$, which then give

$$R_{XX} \approx R_0 + \tfrac{1}{2}\Delta R_{MR}[\sin^2\theta_0 \cos^2\varphi_0 + \Delta\theta \sin 2\theta_0 \cos^2\varphi_0 - \Delta\varphi \sin^2\theta_0 \sin 2\varphi_0 - (\Delta\theta^2 + \Delta\varphi^2)\sin^2\theta_0 \cos^2\varphi_0]. \tag{35}$$

Here, we have kept the second-order terms that scale with $\Delta\theta^2$ and $\Delta\varphi^2$ to show that these terms cannot be neglected when the current induced effective field ΔH_i (that determines the magnitude of $\Delta\theta$ and $\Delta\varphi$) becomes larger. This is because, for a typical geometry that would be employed here (the equilibrium magnetization pointing along the x axis), $\sin(2\theta_0)\sim 0$ and $\sin(2\varphi_0)\sim 0$, and thus the linear terms that scale with $\Delta\theta$ and $\Delta\varphi$ can be smaller than the second-order terms when $\Delta\theta$ or $\Delta\varphi$ become large. As a consequence, there is a limit in ΔH_i above which we cannot neglect the second-order terms and this limit is much smaller than the other geometries described previously. For simplicity, we only consider the small limit of ΔH_i here.

Application of a sinusoidal excitation current $I = \Delta I \sin\omega t$ results in a longitudinal voltage, which is expressed as

$$V_{XX} = R_{XX} I = R_{XX}\Delta I \sin\omega t. \tag{36}$$

Assuming that $\theta_0 = \frac{\pi}{2} \pm \theta_0' \left(\theta_0' \ll 1\right)$, $\varphi\sim\varphi_H$ and the current induced effective field works in sync with the excitation current, Eqs. (35) and (36) give

$$\begin{aligned} V_{XX} &= V_0^{XX} + V_\omega^{XX}\sin\omega t + V_{2\omega}^{XX}\cos 2\omega t \\ V_0^{XX} &= \tfrac{1}{2}\tilde{B}\Delta I, \\ V_\omega^{XX} &= \tilde{A}\Delta I, \\ V_{2\omega}^{XX} &= -\tfrac{1}{2}\tilde{B}\Delta I, \\ \tilde{A} &= R_0 + \tfrac{1}{2}\Delta R_{MR}\cos^2\theta_0'\cos^2\varphi_H, \\ \tilde{B} &= \tfrac{1}{2}\Delta R_{MR}(\mp\Delta\theta\sin 2\theta_0'\cos^2\varphi_H \\ &\quad - \Delta\varphi\cos^2\theta_0\sin 2\varphi_H). \end{aligned} \tag{37}$$

Substituting Eq. (27) into Eqs. (14), (15) and (37) give

$$V_\omega^{XX} = \left\{R_0 + \frac{1}{2}\Delta R_{MR}\cos^2\varphi_H \times\left[1 - \left(\frac{H\cos\theta_H}{H_K - H_A\sin^2\varphi_H - H\sin\theta_H}\right)^2\right]\right\}\Delta I, \tag{38}$$

$$V_{2\omega}^{XX} = \frac{1}{2}\Delta R_{MR}\cos^2\varphi_H \times\left[\frac{H\cos\theta_H\Delta H_Z}{(H_K - H_A\sin^2\varphi_H - H\sin\theta_H)^2}\right]\Delta I. \tag{39}$$

These expressions are similar to those of Eqs. (23) and (24). If we consider that the external field is directed along the z axis, i.e., $\theta_H\sim 0$ or π, then the ratio of the field derivatives of the first and second harmonic signals directly provides the dampinglike term (ΔH_Z):

$$\Delta H_Z = -2\left(\frac{\partial V_{2\omega}^{XX}}{\partial H}\Big/\frac{\partial^2 V_\omega^{XX}}{\partial H^2}\right). \tag{40}$$

Equations (33) and (40) show that combination of the Hall and longitudinal voltage measurements can provide means to evaluate both components of the effective field for in-plane magnetized samples.

2. *Large field sweep*

In material systems with small anisotropic magnetoresistance (AMR), it is difficult to evaluate the dampinglike term using the method described above. To overcome this problem, one can sweep the external field along the film normal and estimate the fieldlike and dampinglike terms from the low- and high-field regimes, respectively. This is a method that combines the approaches described in previous sections: the low-field regime is discussed in Sec. III B 1 a, whereas the high-field regime where the geometry becomes similar to that of the out of plane magnetized system is described in Sec. III A. So far, we have assumed that the equilibrium magnetization is close to either along the film plane or the film normal and the change in θ_0 due to the external field application is small. This assumption allowed us to derive approximate expressions for the first and second harmonic voltage signals. If θ_0 varies with the field in a large way, such approximation cannot be made. Thus here we instead use the first harmonic Hall voltage (V_ω) to estimate θ_0 at each applied field and substitute it into the second harmonic Hall voltage ($V_{2\omega}$) expression.

Substituting Eqs. (14) and (15) into Eq. (19) give to the following expression:

$$\begin{aligned} V_{XY} &= V_0 + V_\omega\sin\omega t + V_{2\omega}\cos 2\omega t \\ V_0 &= \frac{1}{2}(\bar{B}_\theta + \bar{B}_\varphi)\Delta I, \\ V_\omega &= \bar{A}\Delta I, \\ V_{2\omega} &= -\frac{1}{2}(\bar{B}_\theta + \bar{B}_\varphi)\Delta I \\ \bar{A} &= \frac{1}{2}\Delta R_A\cos\theta_0, \\ \bar{B}_\theta &= \frac{1}{2}\frac{\Delta R_A\sin\theta_0\left[\Delta H_Z\sin\theta_0 - (\Delta H_X\cos\varphi_H + \Delta H_Y\sin\varphi_H)\cos\theta_0\right]}{(H_K - H_A\sin^2\varphi_H)\cos 2\theta_0 + H\cos(\theta_H - \theta_0)}, \\ \bar{B}_\varphi &= \frac{\Delta R_P\left(-\Delta H_X\sin\varphi_H + \Delta H_Y\cos\varphi_H\right)\sin^2\theta_0\cos 2\varphi_H}{-H_A\sin\theta_0\cos 2\varphi_H + H\sin\theta_H}. \end{aligned} \tag{41}$$

It turns out that for $\hat{p} = (0, \pm 1, 0)$, it is sufficient to measure the harmonic signals along the x direction, i.e., $\varphi_H = 0$ or π. Then V_ω and $V_{2\omega}$ can be simplified as

$$V_\omega = \frac{1}{2}\Delta R_A \cos\theta_0 \Delta I, \tag{42}$$

$$V_{2\omega} = -\frac{\Delta R_A}{2}\left[\frac{1}{2}\frac{\sin\theta_0\cos\varphi_H}{H_K\cos 2\theta_0 + H\cos(\theta_H - \theta_0)}a_J + \xi\frac{\sin^2\theta_0\cos\varphi_H}{-H_A\sin\theta_0 + H\sin\theta_H}b_J\right]\Delta I, \tag{43}$$

where we have used a_J and b_J from Eq. (21) and $\xi \equiv \frac{\Delta R_P}{\Delta R_A}$ as before. To obtain Eq. (43), we first note from Eq. (21) that

$$\Delta\vec{H} = (\Delta H_X, \Delta H_Y, \Delta H_Z) = (-a_J\cos\theta_0, b_J, a_J\sin\theta_0\cos\varphi_H) \quad \text{for } \hat{p} = (0,1,0). \tag{44}$$

Using Eq. (44), the expression inside the square bracket of the numerator in $\bar{B}_\theta$ [Eq. (41)] can be simplified, that is, $\Delta H_Z \sin\theta_0 - \Delta H_X \cos\varphi_H \cos\theta_0 = a_J \cos\varphi_H$ (we assume $\varphi_H = 0$ or π). Substituting these expressions into Eq. (41) yields Eq. (43). Equation (43) takes a form similar to that of Eq. (29): the first term depends on a_J and ΔR_A but its contribution is small unless $H \sim |H_K|$ or larger. The second term is proportional to b_J and ΔR_P and dominates $V_{2\omega}$ at low fields. Thus the low-field values of $V_{2\omega}$ provide information of b_J, whereas the higher-field values give a_J.

To estimate a_J and b_J experimentally, we use the measured V_ω and Eq. (42) to evaluate θ_0 at each H. The H dependence of V_ω also provides value of $\Delta R_A \Delta I$ and information on H_K. H_K can be roughly estimated by extrapolating a linear fitting of V_ω versus H near zero field to the saturation value of V_ω at large fields (the intersection field is $\sim H_K$), as commonly done in estimating H_K using magnetization hysteresis loops. At each H, one can substitute θ_0 obtained from the V_ω versus H curve into Eq. (43) and fit $V_{2\omega}$ versus H with a_J and b_J as the fitting parameters. It should be noted that when the field direction is reversed in one field sweep, it is not appropriate to substitute a *negative* H in Eq. (43); rather one needs to change θ_0, θ_H, φ_H to $\pi - \theta_0$, $\pi - \theta_H$, $\varphi_H + \pi$, respectively, and keep H positive. In effect, this will result in changing the sign of $V_{2\omega}$ for negative fields.

As described in Sec. II C, possible magnetization angular dependence of a_J and b_J can influence the fitting process here as the change in the magnetization angle (θ_0) is large, i.e., the magnetization direction changes from in-plane to out of plane orientation. In general, one can include the angular (θ_0, φ_0) dependence of a_J and b_J in Eq. (21), and consequently in Eq. (43), and fit the field (H) dependence of $V_{2\omega}$ with a magnetization angle-independent effective field components as fitting parameters. For simplicity, here we assume a_J and b_J to be constant, i.e., they do not depend on the relative angle between the magnetization and the current flow direction [or $\hat{p}$ in Eq. (21)].

IV. COMPARISON TO NUMERICAL CALCULATIONS

The analytical solutions derived above are compared to numerical calculations. We solve Eq. (21) numerically to obtain the equilibrium magnetization direction and the associated harmonic voltage signals. A macrospin model [36,37] is used to describe the system. Substituting Eq. (1) into Eq. (21), the following differential equations are obtained:

$$\begin{aligned}
\frac{1+\alpha^2}{\gamma}\frac{\partial\theta}{\partial t} &= \alpha h_\theta + h_\varphi, \\
\frac{1+\alpha^2}{\gamma}\frac{\partial\varphi}{\partial t}\sin\theta &= -h_\theta + \alpha h_\varphi \\
h_\theta &= a_J\cos\varphi + b_J\cos\theta\sin\varphi + h_X\cos\theta\cos\varphi \\
&\quad + h_Y\cos\theta\sin\varphi - h_Z\sin\theta, \\
h_\varphi &= a_J\cos\theta\sin\varphi + b_J\cos\varphi - h_X\sin\varphi \\
&\quad + h_Y\cos\varphi, \\
h_X &= H_X - M_S N_X\sin\theta\cos\varphi, \\
h_Y &= H_Y - M_S N_Y\sin\theta\sin\varphi, \\
h_Z &= H_Z - (M_S N_Z - H_K)\cos\theta.
\end{aligned} \tag{45}$$

The two coupled differential equations are numerically solved to obtain the equilibrium magnetization direction when both the external and the current induced effective fields are turned on. To mimic the experimental setup, a sinusoidal current is passed along the x axis and the resulting Hall and longitudinal voltages are evaluated. Contributions from the anomalous Hall effect (AHE) and the planar Hall effect (PHE) are considered for the Hall voltage and the anisotropic magnetoresistance (AMR) is taken into account for the longitudinal voltage. For a given time during one cycle of the sinusoidal current application, we calculate the equilibrium magnetization direction and the corresponding Hall and longitudinal voltages. One cycle is divided into two hundred time steps to obtain the temporal variation of the Hall and longitudinal voltages. The calculated voltages are fitted with Eq. (19) ($V_{XY} = V_0 + V_\omega \sin\omega t + V_{2\omega}\cos 2\omega t$) or Eq. (37) ($V_{XX} = V_0^{XX} + V_\omega^{XX}\sin\omega t + V_{2\omega}^{XX}\cos 2\omega t$) to obtain the first and second harmonic signals. We compare the numerical results with the analytical solutions derived in the previous sections.

A. Out-of-plane magnetization systems

Figure 2 shows results for the out of plane magnetized samples. The equilibrium magnetization angle (θ_0) with respect to the film normal, first and second harmonic Hall voltages are plotted against an in-plane field directed along the current flow direction (i.e., along the x axis) in Figs. 2(a), 2(b), and 2(d), respectively. The transverse field (directed along the y axis) dependence of the second harmonic Hall voltage is shown in Fig. 2(f); the corresponding magnetization angle (θ_0) and the first harmonic Hall voltage are the same with those shown in Figs. 2(a) and 2(b), respectively. The material parameters used here are typical of perpendicularly magnetized heterostructures (see Fig. 2 caption for the details). The open symbols represent results from the numerical calculations (squares: magnetization pointing $+z$, circles: magnetization along $-z$) whereas the solid/dashed lines correspond to the analytical results. As evident, the analytical solutions agree well with the numerical results.

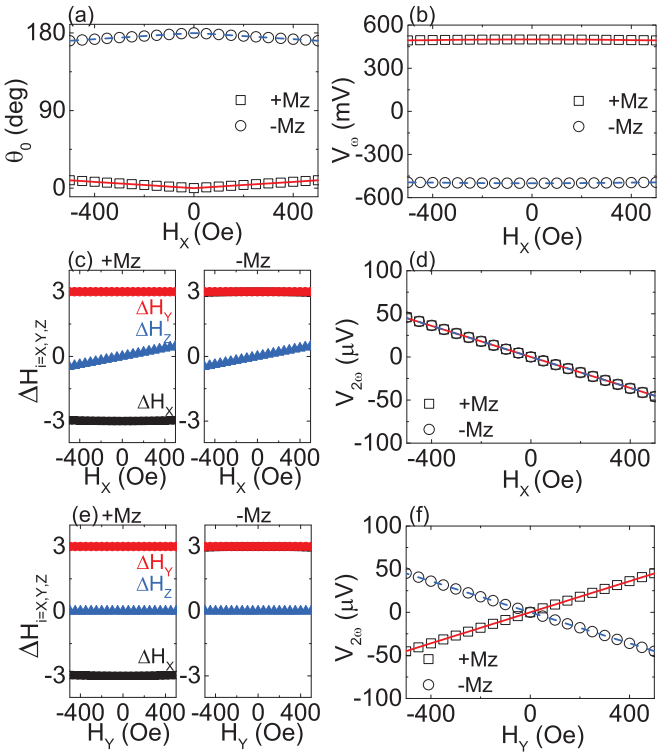

FIG. 2. (Color online) (a) Magnetization angle with respect to the film normal (θ_0), (b) first harmonic Hall voltage and (d) and (f) second harmonic Hall voltage plotted against in-plane external field ($\theta_H = 90°$). The field is directed along the x axis ($\varphi_H = 0°$) for (a), (b), and (d) and along the y axis ($\varphi_H = 90°$) for (f). Open symbols show numerical calculations using the macrospin model. Solid/dashed lines represent the analytical solutions: (a) Eq. (22), (b) Eq. (23), (d) and (f) Eq. (24). (c) and (e) x, y, and z components of the effective field used for the numerical calculations. Left (right) panel indicates the effective field when the magnetization is pointing along $+z$ ($-z$). Parameters used in the numerical calculations: $H_K = 3162$ Oe, $H_A = -6$ Oe, $\alpha = 0.01$, $\gamma = 17.6$ MHz/Oe, $a_J = 3$ Oe, $b_J = 3$ Oe, $\hat{p} = (0,1,0)$, $\Delta R_A = 1\ \Omega$, $\Delta R_P = 0.1\ \Omega$, $\Delta I = 1$ A.

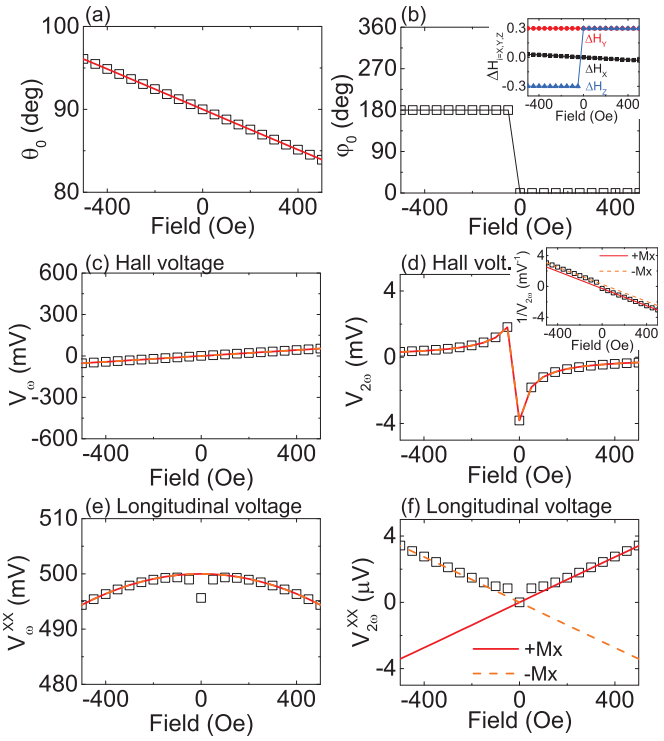

FIG. 3. (Color online) (a) Polar (θ_0) and (b) azimuthal (φ_0) angles of the magnetization, (c) first and (d) second harmonic Hall voltages (V_{XY}), (e) first and (f) second harmonic longitudinal voltages (V_{XX}) as a function of a slightly tilted out of plane field ($\theta_H = 5°$). The in-plane component of the tilted field is directed along the x axis ($\varphi_H = 0°$). Open symbols show numerical calculations using the macrospin model. Solid lines represent the analytical solutions: (a) and (b) Eq. (27), (c) Eq. (28), (d) Eq. (30), (e) Eq. (38), (f) Eq. (39). Inset of (b) shows the x, y, and z components of the effective field used for the numerical calculations. Parameters used in the numerical calculations: $H_K = -4657$ Oe, $H_A = -4$ Oe, $\alpha = 0.01$, $\gamma = 17.6$ MHz/Oe, $a_J = 0.3$ Oe, $b_J = 0.3$ Oe, $\hat{p} = (0,1,0)$, $\Delta R_A = 1\ \Omega$, $\Delta R_P = 0.1\ \Omega$, $\Delta R_{MR} = 1\ \Omega$, $R_0 = 0\ \Omega$, $\Delta I = 1$ A.

The x, y, and z components of the current induced effective field are shown in Figs. 2(c) and 2(e) when the in-plane field is swept along x and y axes, respectively. We use $\hat{p} = (0,1,0)$, $a_J = 3$ Oe and $b_J = 3$ Oe. At low magnetic field, one can consider ΔH_X and ΔH_Y representing a_J and b_J, respectively, [see Eq. (44)]. We test the validity of Eq. (26) by fitting the external field dependence of the first and second harmonic voltages with parabolic and linear functions, respectively, and calculate quantities corresponding to B_X and B_Y [Eq. (25)]. Substituting B_X and B_Y into Eq. (26), we obtain $\Delta H_X \sim -3.03$ Oe and $\Delta H_Y \sim 2.99$ Oe, which match well with a_J and b_J used in the numerical calculations.

B. In-plane magnetization systems

1. Low field limit

Numerical results of in-plane magnetized systems for the low-field limit are shown in Fig. 3. The material parameters used are relevant for in-plane magnetized systems with a small perpendicular magnetic anisotropy ($H_K \sim -4500$ Oe).

Figure 3 shows results when an out of plane external field, slightly tilted ($\theta_H = 5°$) from the film normal, is applied. The in-plane component of the tilted field is directed along the magnetic easy axis, which is the x axis here ($\varphi_H = 0°$, the in-plane anisotropy field (H_A) is $\sim$–4 Oe). The open symbols represent the numerical results. The equilibrium magnetization angles (θ_0, φ_0) are plotted against the slightly tilted out of plane field in Figs. 3(a) and 3(b), respectively. The magnetization direction reverses [Fig. 3(b)] due to the in-plane component of the tilted field. Figures 3(c) and 3(d) show the first and second harmonic Hall voltages whereas Figs. 3(e) and 3(f) display the first and second harmonic longitudinal voltages. The solid lines represent the analytical solutions, which agree well for the Hall voltages [Figs. 3(c) and 3(d)] but show a small deviation at low fields for the longitudinal voltages [Figs. 3(e) and 3(f)]. The deviation is due to the nonlinear (higher order) terms in R_{XX} [Eq. (35)].

To reduce contributions from the nonlinear terms in R_{XX}, we have used $a_J = 0.3$ Oe and $b_J = 0.3$ Oe to generate the effective field in Fig. 3 [$\hat{p} = (0,1,0)$ is assumed as before]. For $a_J = 3$ Oe and $b_J = 3$ Oe, as used in the calculations shown in

Fig. 2, the nonlinear terms dominate the harmonic longitudinal voltages, i.e., the analytical solutions do not match the numerical calculations in this external field range (the solution shows better agreement when the external field range is expanded). Note that such effect is negligible for the harmonic Hall voltages [Figs. 3(c) and 3(d)] for $a_J = 3$ Oe and $b_J = 3$ Oe. The resulting components of the current induced effective field ΔH_i are shown in the inset of Fig. 3(b). One can identify that ΔH_Z is the dampinglike term, which changes its sign upon magnetization reversal, and ΔH_Y is the fieldlike term. Since the magnetization lies within the film plane, ΔH_X is nearly zero.

We fit the numerically calculated harmonic Hall voltages versus external field (H) with a linear function and use Eq. (33) to estimate ΔH_Y [see Fig. 3(d) inset for $V_{2\omega}^{-1}$ versus H and the corresponding linear fit]. We obtain $\Delta H_Y \sim 0.32$ Oe for both magnetization direction (pointing along $+x$ and $-x$). This agrees well with b_J used in the numerical calculations.

For the harmonic longitudinal voltages, we use Eq. (40) to obtain ΔH_Z. Fitting the external field dependence of the first and second harmonic signals with parabolic and linear functions, respectively, we find $\Delta H_Z \sim 0.30$ and ~ -0.30 Oe for magnetization pointing along $+x$ and $-x$, respectively. Although these values match that of a_J, it should be noted that nonlinear effects start to take place when a_J and b_J becomes large. Since the nonlinear terms become apparent when the external field is small, it is desirable to fit the respective curvature and slope of V_ω and $V_{2\omega}$ at higher fields (but much smaller than $|H_K|$).

2. *Large field sweep*

We next show the validity of solutions (42) and (43) by comparing them to numerical calculations. Solid symbols of Fig. 4 show results from the numerical calculations. The external field is directed nearly along the film normal ($\theta_H = 5°$) and we apply large enough field to force the magnetic moments to point out of plane. The symbols in Figs. 4(a) and 4(b) show the external field dependence of the equilibrium polar angle of the magnetization and the first harmonic voltage V_ω. The solid line in Fig. 4(a) is calculated from the numerical data shown in Fig. 4(b) using Eq. (42), i.e., $\theta_0 = \cos^{-1}(V_\omega / \frac{1}{2}\Delta R_A \Delta I)$. Here, we take the value of $\Delta R_A \Delta I$ used in the numerical calculations to obtain θ_0 (in experiments, we need to estimate $\Delta R_A \Delta I$ by measuring V_ω versus H at $\theta_H = 0°$). Figures 4(c) and 4(d) show the second harmonic voltage ($V_{2\omega}$) as a function of the external field for $a_J = 3$ Oe, $b_J = 3$ Oe and $a_J = 3$ Oe, $b_J = -3$ Oe, respectively. The resulting x, y, and z components of the effective field are shown in Figs. 4(e) and 4(f): $\hat{p} = (0,1,0)$ as before.

As described in the previous section, the $\sim 1/H$ dependence of $V_{2\omega}$ at low field is due to contribution from the fieldlike term (ΔH_Y, or b_J) via the planar Hall effect. Indeed, $V_{2\omega}$ reverses its sign at low field when Figs. 4(c) and 4(d) are compared owing to the difference in the sign of b_J. In addition, one can observe a shoulder and a humplike features in Figs. 4(c) and 4(d), respectively, when $H \sim \pm|H_K|$ ($H_K \sim -4600$ Oe in Fig. 4). Such feature is due to the first term in Eq. (43), which is related to the presence of the dampinglike term (a_J), that dominates over the second term when $H \sim \pm|H_K|$. We substitute H_K, θ_H, φ_H, $\Delta R_A \Delta I$, ξ used in the numerical calculations and θ_0 obtained from V_ω [Fig. 4(b)] to Eq. (43) and fit $V_{2\omega}$ versus H with a_J and b_J as fitting parameters. The results are shown by

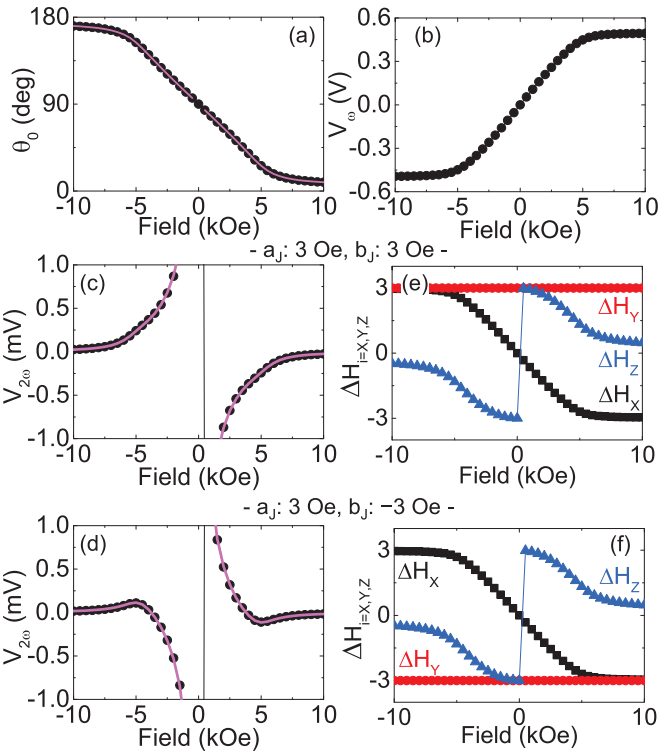

FIG. 4. (Color online) (a) Polar (θ_0) angle of the magnetization, (b) first and (c) and (d) second harmonic Hall voltages as a function of a slightly tilted out of plane field ($\theta_H = 5°$). The in-plane component of the tilted field is directed along the x axis ($\varphi_H = 0°$). Solid symbols show numerical calculations using the macrospin model. Solid lines represent the analytical solutions: (a) Eq. (42), (c) and (d) Eq. (43). (e) and (f) x, y, and z components of the effective field used for the numerical calculations. Parameters used in the numerical calculations: $H_K = -4561$ Oe, $H_A = -4$ Oe, $\alpha = 0.01$, $\gamma = 17.6$ MHz/Oe, $\hat{p} = (0,1,0)$, $\Delta R_A = 1\,\Omega$, $\Delta R_P = 0.1\,\Omega$, $\Delta R_{MR} = 1\,\Omega$, $R_0 = 0\,\Omega$, $\Delta I = 1$ A. (c,e) $a_J = 3$ Oe, $b_J = 3$ Oe, (d,f) $a_J = 3$ Oe, $b_J = -3$ Oe.

the solid lines in Figs. 4(c) and 4(d), which agree well with the numerical calculations. The fitting results give $a_J \sim 2.90$ Oe and $b_J \sim 3.08$ Oe for Fig. 4(c) and $a_J \sim 3.10$ Oe and $b_J \sim -3.08$ Oe for Fig. 4(d) that are not far from the nominal values used in the numerical calculations. Thus these results show that one can estimate the dampinglike (a_J) and the fieldlike (b_J) terms for in-plane magnetized samples by sweeping the field along the film normal direction.

V. EXPERIMENTAL RESULTS

We study two different film structures to evaluate the current induced effective field using the formula provided above. In particular, we show results from in-plane magnetized samples as this system has not been evaluated in detail previously. The two film structures are Sub|3 Pt|1 CoFeB|2 MgO|1 Ta and Sub|10 CuIr|t_{CoFeB} CoFeB|2 MgO|1 Ta. The thickness (t_{CoFeB}) of the CoFeB layer in the latter film varies from $\sim$1–3 nm in the substrate (the CoFeB layer forms a wedge): here we use $t_{\mathrm{CoFeB}} \sim 1.3$ nm. Both samples are annealed at 300 °C for one hour. The CuIr underlayer film [27] is annealed under the application of in-plane field (4 kOe) along the x axis in Fig. 1.

No field is applied during the annealing for the Pt underlayer film. Both underlayers (Pt and CuIr) have been reported to possess the same sign of the spin Hall angle (γ_{SH}): $\gamma_{SH}\sim0.01$–0.07 for Pt [38–41] and $\gamma_{SH}\sim0.02$–0.03 for CuIr [27,42]. For the CuIr underlayer films the current induced effective field has been estimated using spin torque switching phase diagram measurements [27], thus giving a reference for comparison. As Pt underlayers typically promote in-plane anisotropy for CoFeB|MgO, we choose this material as a comparison to CuIr.

Hall bars are patterned from the films using conventional optical lithography and Ar ion etching. 10 Ta|100 Au or 10 Cr|100 Au (in nanometers) electrodes are formed by lift-off processes. The width of the Hall bar is ~10 μm: the device structure is similar to that reported previously [23]. We apply a constant amplitude sinusoidal voltage (amplitude: V_{IN}, frequency$\sim$507.32 Hz) to the Hall bar. Since the Hall bar longitudinal resistance (R_{XX}) shows little dependence on the applied voltage, the source can be considered as a constant amplitude sinusoidal current (ΔI) source. Lock-in amplifiers are used to measure the in-phase first and the out of phase second harmonic voltages simultaneously. We use experimentally determined values of $\xi\equiv\frac{\Delta R_P}{\Delta R_A}:\sim0.1$ for Sub|3 Pt|1 CoFeB|2 MgO|1 Ta and ~0.05 for Sub|10 CuIr|$\sim$1.3 CoFeB|2 MgO|1 Ta.

A. Pt|CoFeB|MgO

Figure 5(a) shows in-plane and out of plane magnetization hysteresis loops of Sub|3 Pt|1 CoFeB|2 MgO|1 Ta (nm) measured using vibrating sample magnetometry (VSM). The easy axis is oriented along the film plane and $H_K\sim-2000$ Oe. Owing to the perpendicular magnetic anisotropy originating at the CoFeB|MgO interface [43], H_K is significantly reduced in magnitude from $4\pi M_S$. Figure 1(b) shows the first harmonic voltage plotted as a function of the external field swept along near the z axis with different tilt angles: $\theta_H\sim0°$ (black squares), $\theta_H\sim-9°$ (pink circles) and $\theta_H\sim+9°$ (brown triangles). Note that here we use negative polar angles for convenience. In polar coordinates ($0\leqslant\theta_H\leqslant\pi$ and $0\leqslant\varphi_H\leqslant2\pi$), $\theta_H\sim-9°$ (and an arbitrary φ_H) corresponds to $\theta_H\sim9°$ and $\varphi_H\rightarrow\varphi_H+\pi$; the latter should be substituted in the equations. The in-plane component of the external field is directed along the x axis (i.e., $\varphi_H\sim0$). The estimated H_K for $\theta_H\sim0°$ more or less agrees with that of the VSM measurements [Fig. 5(a)].

The field dependence of the second harmonic voltages are shown in Figs. 5(c)–5(e) for the three field tilt angles ($\theta_H\sim0°$, 9°, −9°). When the tilt angle is nonzero, we obtain a curve similar to that of the analytical and numerical calculations shown in Fig. 4(d). Note that the sign of $V_{2\omega}$ reverses when the tilt direction (θ_H) is reversed. This is in accordance with Eq. (30) [or Eq. (43)]. The 0 degree tilt curve should be ideally constant with the external field, however, multidomain formation at low fields and/or a small misalignment of the field may create features as shown in Fig. 5(d).

We use Eq. (43) to fit $V_{2\omega}$ versus H for nonzero θ_H: exemplary fitting results are shown by the solid lines in Figs. 5(c) and 5(e). The fitting parameters are a_J, b_J (and an offset voltage which is typically less than ~1 μV) and we use V_ω versus H [Fig. 5(b)] to obtain θ_0 at each H. The obtained a_J and b_J are shown in Figs. 5(f) and 5(g) as a function of the input voltage amplitude V_{IN} for $\theta_H\sim9°$. To show the magnetization direction dependence of the dampinglike and fieldlike terms, a_J and b_J are converted to ΔH_Z and ΔH_Y using Eq. (44), respectively, when the magnetization points along the x axis.

Both components of the effective field, ΔH_Z and ΔH_Y, linearly scales with V_{IN}. The slope of $\Delta H_{Z(Y)}$ versus V_{IN} is plotted in Figs. 5(h) and 5(i) as a function of the field tilt angle θ_H for the dampinglike and fieldlike terms, respectively.

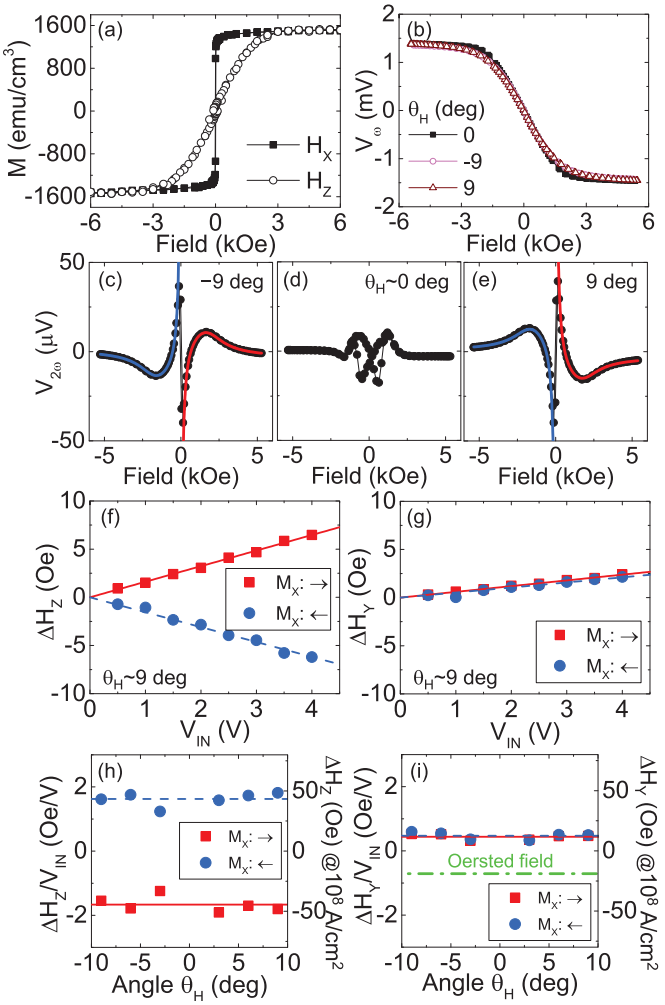

FIG. 5. (Color online) Experimental results for Sub|3 Pt|1 CoFeB|2 MgO|1 Ta (in nanometers). (a) Magnetization hysteresis loops: open and solid symbols represent out of plane (H_z) and in-plane (H_X) field sweeps, respectively. (b) First harmonic voltage as a function of external field with different tilt angles (θ_H). $V_{IN}=0.5$ V. (c)–(e) External field dependence of the second harmonic voltage ($V_{2\omega}$) for three different θ_H. $V_{IN}=3.5$ V. The solid lines represent fitting results using Eq. (43). (f) and (g) The dampinglike term ΔH_Z and the fieldlike term ΔH_Y obtained from the fitting of $V_{2\omega}$ plotted against the excitation voltage amplitude (V_{IN}) for $\theta_H\sim9°$. (h) and (i) θ_H dependence of the effective field per unit excitation voltage amplitude for ΔH_Z and ΔH_Y. The right axis shows the corresponding effective field if a current density of 1×10^8 A/cm^2 were applied to the underlayer (3-nm Pt). Squares and circles in (f)–(i) represent the corresponding effective field for magnetization pointing along $+x$ and $-x$ axes, respectively. The green dashed line in (i) show the calculated Oersted field if all the current flows into the underlayer. The field is calculated for 1 nm above the top surface of the Pt underlayer.

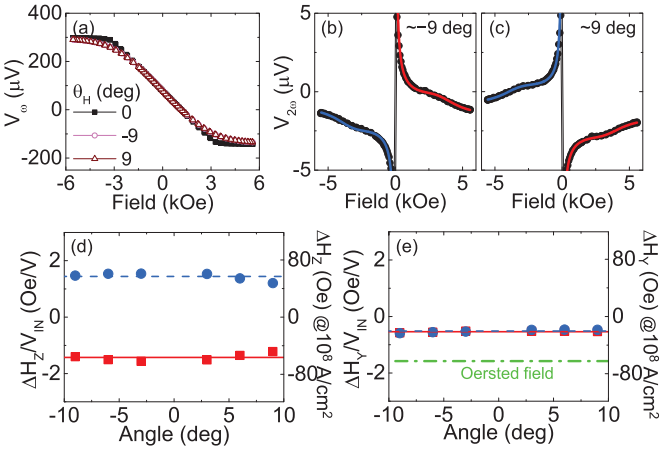

FIG. 6. (Color online) Experimental results for Sub|10 CuIr|∼1.3 CoFeB|2 MgO|1 Ta (in nanometers). (a) First harmonic voltage as a function of external field with different tilt angles (θ_H). $V_{IN} = 0.5$ V. (b) and (c) External field dependence of the second harmonic voltage ($V_{2\omega}$) for $\theta_H \sim -9°$ (b) and 9° (c). $V_{IN} = 3.5$ V. The solid lines represent fitting results using Eq. (43). (d) and (e) θ_H dependence of the effective field per unit excitation voltage amplitude for the dampinglike term ΔH_Z and the fieldlike term ΔH_Y. The right axis shows the corresponding effective field if a current density of 1×10^8 A/cm^2 were applied to the underlayer (10-nm CuIr). Squares and circles represent the corresponding effective field for magnetization pointing along $+x$ and $-x$ axes, respectively. The green dashed line in (e) show the calculated Oersted field if all the current flows into the underlayer. The field is calculated for 1 nm above the top surface of the CuIr underlayer.

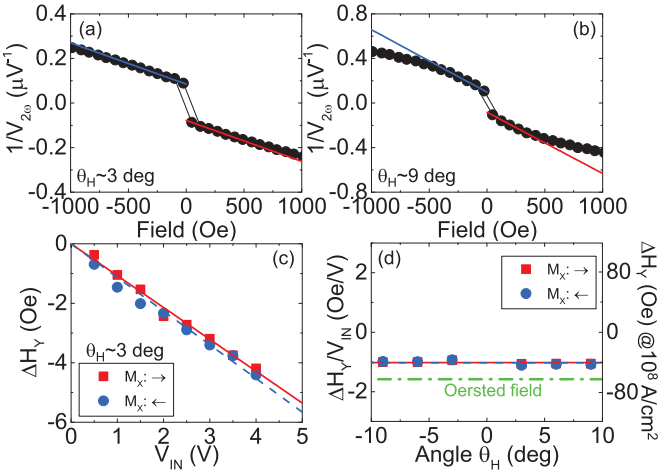

FIG. 7. (Color online) Experimental results for sub|10 CuIr|∼1.3 CoFeB|2 MgO|1 Ta (in nanometers). (a) and (b) External field dependence of the inverse of the second harmonic voltage ($1/V_{2\omega}$) for $\theta_H \sim 3°$ (a) and 9° (b). The solid lines represent linear fitting to the data. $V_{IN} = 3.5$ V. (c) ΔH_Y, obtained from the fitting and Eq. (33), plotted against the excitation voltage amplitude (V_{IN}) for $\theta_H \sim 3°$. (d) θ_H dependence of the effective field per unit excitation voltage amplitude for the fieldlike term, ΔH_Y. The right axis shows the corresponding effective field if a current density of 1×10^8 A/cm^2 were applied to the under-layer (10-nm CuIr). Squares and circles represent the corresponding effective field for magnetization pointing along $+x$ and $-x$ axes, respectively. The green dashed line in (d) show the calculated Oersted field if all the current flows into the underlayer [same as in Fig. 6(e)].

The corresponding effective field if current, density of 1×10^8 A/cm^2, were to flow in the Pt underlayer is shown in the right axis. $\Delta H_Z \sim -44$ Oe when both the magnetization and the current are directed along $+x$; the direction of ΔH_Z is consistent with the sign of the spin Hall angle associated with the Pt underlayer [38–41]. For ΔH_Y, we show the size of the Oersted field (see Appendix for the calculations) generated when the same magnitude of current is passed through the Pt underlayer. Figure 5(i) shows that ΔH_Y due to the spin-orbit torque is directed along $+y$ when current is passed along the $+x$ axis and is opposite to that of the Oersted field. Its magnitude is the difference between the measured ΔH_Y ($\sim$12 Oe) and the estimated Oersted field (~ -18 Oe), which is $\sim$30 Oe. This is comparable to that of the dampinglike term (ΔH_Z), however, the fieldlike term is directed in way that the torque associated with it opposes that of the dampinglike term for current induced magnetization switching [31], i.e., the fieldlike term points opposite to the incoming electron's spin direction (assuming that the spin Hall effect is the source of the current induced effective field and its sign is in accordance with previous reports [38–41]).

B. CuIr|CoFeB|MgO

Similar experiments are carried out for the CuIr underlayer films. The field dependence of the first harmonic voltage is shown in Fig. 6(a). $\Delta R_A \Delta I$ is smaller than that of the Pt underlayer films since the shunt current through the underlayer is larger. The second harmonic voltages are plotted against the field in Figs. 6(b) and 6(c) for two field tilt angles, $\theta_H \sim -9°$and 9°, respectively. In contrast to what have been observed for the Pt underlayer films, here we observe a shoulder instead of a hump at $H \sim \pm|H_K|$, a feature similar to that obtained by the analytical and numerical calculations shown in Fig. 4(c). Again we use Eq. (43) to fit the $V_{2\omega}$ versus H curve to estimate a_J and b_J. The slope of the obtained a_J, b_J versus V_{IN} are plotted shown in Figs. 6(d) and 6(e) for the dampinglike and fieldlike terms, respectively, as a function the field tilt angle θ_H. As before, we convert a_J and b_J to ΔH_Z and ΔH_Y to show the magnetization direction dependence of the effective field explicitly. For magnetization pointing along $+x$, we find ΔH_Z to be ~ -57 Oe and ΔH_Y to be ~ -21 Oe for current flowing along $+x$. Taking into account the estimated Oersted field (~ -63 Oe) shown by the green dash-dotted line in Fig. 6(e), ΔH_Y due to the spin-orbit torque is $\sim$42 Oe. Both components (ΔH_Z and ΔH_Y) point along the same direction as that of the Pt underlayer film, which is consistent with the sign of the spin Hall angle of the CuIr underlayer [27,42]. Similar to the Pt|CoFeB|MgO system, the fieldlike term points opposite to the incoming electron's spin direction.

We can use the same data set shown in Fig. 6 to test Eq. (33) in evaluating the fieldlike term (ΔH_Y). The inverse of $V_{2\omega}$ is plotted against H in Figs. 7(a) and 7(b) for field tilt angles of $\sim 3°$ and $\sim 9°$, respectively. A small offset voltage of ~ 1 μV is subtracted before taking the inverse of $V_{2\omega}$. To evaluate $\partial(1/V_{2\omega})/\partial H$ in Eq. (33), we fit $1/V_{2\omega}$ versus H in the low-field regime with a linear function: the fitting results are shown by the solid lines in Figs. 7(a) and (7b). It is evident that $1/V_{2\omega}$

deviates from a linear function of H at smaller fields for larger θ_H. It is thus preferable to limit θ_H to a smaller value when performing this analysis.

The low-field part ($|H| \leq \sim 1000$ Oe) of V_ω is fitted with a linear function to obtain $\partial V_\omega/\partial H$. Substituting $\partial V_\omega/\partial H$, $\partial(1/V_{2\omega})/\partial H$, θ_H and the same H_K used in Fig. 6 into Eq. (33), we evaluate ΔH_Y at different θ_H. The input voltage (V_{IN}) dependence of ΔH_Y is plotted in Fig. 7(c) for $\theta_H \sim 3°$. The squares and circles represent the respective ΔH_Y values when the external field (H) is positive and negative (the corresponding x component of the magnetization (M_X) is positive and negative, respectively). The slope of ΔH_Y versus V_{IN} is shown against θ_H in Fig. 7(d). Although the inverse of $V_{2\omega}$ shows a nonlinear H dependence at higher fields for larger θ_H [e.g., Fig. 7(b)], $\Delta H_Y/V_{IN}$ shows rather small θ_H dependence. The mean value of $\Delta H_Y/V_{IN}$ is ~ -41 Oe (for current density of 1×10^8 A/cm^2 flowing through the CuIr underlayer), which is larger in magnitude than that shown in Fig. 6(e). Taking into account the Oersted field (~ -63 Oe), ΔH_Y due to the spin-orbit torque amounts to ~ 22 Oe.

We compare the size of the dampinglike and fieldlike terms with those reported previously [27] using spin torque switching phase diagram measurements: the dampinglike and the fieldlike effective fields are reported to be ~ -51 and ~ 14 Oe, respectively, when 1×10^8 A/cm^2 of current density flows through the CuIr underlayer. The dampinglike term estimated here [~ -57 Oe, Fig. 6(d)] agrees well with that of Ref. [27]. However, the difference in the fieldlike term is rather large, particularly for the former analysis using the large field range [~ 42 Oe, Fig. 6(e)]. The latter analysis using the low-field regime [~ 22 Oe, Fig. 7(d)] shows better agreement. It is possible that the recently reported angular dependence (the relative angle between the current and the magnetization directions) of the fieldlike term [24], which is reported to be much larger than that of the dampinglike term, may influence the fitting of $V_{2\omega}$ for a large field sweep. To include this effect, one needs to introduce the appropriate angular dependence of a_J and b_J in Eqs. (21) and (43) and fit $V_{2\omega}$ versus H using angular-*independent* fitting parameters. The discrepancy of the fieldlike term (ΔH_T) for the two analyses we present here [Eqs. (33) and (43)] requires further investigation for clarification.

We note that it is difficult to evaluate ΔH_Y using the small field analysis [Eq. (33)] for the Pt underlayer films as the inverse of $V_{2\omega}$ diverges at $|H| \sim \pm|H_K|/2$ and influences the linear fitting of the low field regime. Similarly, since CoFeB shows small anisotropic magnetoresistance, the second harmonic longitudinal voltage is too small to resolve its field dependence. We thus conclude that, for the systems studied here, fitting the second harmonic voltage for a large field range using Eqs. (42) and (43) provides a better solution in evaluating the current induced effective field.

C. Discussion

The effective field we find in Pt|CoFeB|MgO is rather small [~ 44 Oe when $\sim 10^8$ A/cm^2 of current density is passed in the Pt layer, Fig. 5(h)] compared to what have been reported in the literature. For example, Emori *et al.* [25] find the dampinglike term to be ~ 500 Oe in 3 Ta|3 Pt|0.6 CoFe|1.8 MgO|2 Ta and Garello *et al.* [24] report ~ 690 Oe in 3 Pt|0.6 Co|2 AlOx. Our value is somewhat closer to that reported by Liu *et al.* [38] (~ 174 Oe in 2 Pt|0.6 Co|AlOx), but still more than three times smaller. We find values of the dampinglike term in 3 Pt|0.6 Co|1 MgO (nm) smaller than what we report here. The Co layer in 3 Pt|0.6 Co|1 MgO is magnetized along the film normal (results will be reported elsewhere), thus we consider the small values we find here is somewhat related to the Pt layer we use. To clarify the differences, it is essential to study the Pt layer thickness dependence of the effective field and estimate the spin diffusion length of this material, which varies from ~ 1 to ~ 10 nm depending on the measurement methods and perhaps on the film structure and its quality [41].

As noted above, the fieldlike term is pointing against the incoming spin direction, assuming that the spin Hall effect is the source of the fieldlike term and its sign is in accordance with previous reports. This seems to be a common feature in magnetic heterostructures with asymmetric interfaces, e.g., an ultrathin magnetic layer sandwiched between a heavy metal layer and an oxide layer [23–25,27]. Such fieldlike term can hinder the magnetization switching process triggered by the dampinglike term. Note that the fieldlike term here scales linearly with the input current, which should be distinguished from the dominant fieldlike torque found in magnetic tunnel junctions (MTJs) that scales with the *square* of the bias voltage [44–46]. The direction of the MTJ fieldlike term that is *linear* with the bias voltage seems to be more random: it can point either parallel or antiparallel to the incoming spin direction [46–49].

The size of the fieldlike term seems to depend considerably on the interface between the heavy nonmagnetic metal (NM) and the ferromagnetic (FM) layers. The fieldlike term is much smaller than the dampinglike term in the CuIr underlayer films [27], whereas the trend is opposite for the Ta underlayer films (the fieldlike term is $\sim$2–3 times larger than the dampinglike term) [23]. If the spin Hall torque is the source of the fieldlike term, these results indicate that how spins transmit across the NM|FM interface is quite different depending on the underlayer material used. In particular, a large fieldlike term suggests that the diffusing electrons' spin rotate at the interface in a rather coherent way so that electrons with different wave vectors contribute to the rotation constructively [50,51]. Identifying the origin of the fieldlike term, including the Rashba-Edelstein effects discussed previously [9–16,24], is particularly important for device applications [16,17] that utilize current induced switching in magnetic heterostructures.

VI. CONCLUSION

We have derived analytical formulas that describe the adiabatic (low-frequency) harmonic Hall and longitudinal voltages measurements when current induced spin-orbit torques develop in magnetic heterostructures. We treat both out of plane and in-plane magnetized samples, taking into account the anomalous and planar Hall effects for the Hall voltage measurements and the anisotropic mangnetoresistance for the longitudinal voltage measurements. The derived forms are compared to numerical calculations using a macrospin model and show good agreement. We experimentally characterize two different in-plane magnetized systems, Pt|CoFeB|MgO and CuIr|CoFeB|MgO, and apply the developed formula to evaluate the effective field in each system. The effective field obtained for the latter system shows relatively good

agreement with that evaluated using a spin torque switching phase diagram measurements. Utilizing the harmonic voltage measurements can help gaining solid understanding of the spin-orbit torques, which is key to the development of ultrathin magnetic heterostructures for advanced storage class memories and logic devices.

ACKNOWLEDGMENTS

M. H. thanks Kevin Garello and Kyung-Jin Lee for fruitful discussions which stimulated this work. We acknowledge Jaivardhan Sinha for sample preparation and Seiji Mitani for helpful discussions. This work was partly supported by the Grant-in-Aid (25706017) from MEXT and the FIRST program from JSPS.

APPENDIX

1. Derivation of the analytical solutions

Here, we describe how Eqs. (14) and (15) are derived. Substituting Eqs. (12) and (13) into Eqs. (8) and (9) gives the following expressions for the modulation amplitudes of the magnetization angle:

$$\Delta\theta = \frac{1}{F_1}\left[(\cos\theta_0\cos\varphi_0 - C\sin\theta_0\sin\varphi_0)\,\Delta H_X + (\cos\theta_0\sin\varphi_0 + C\sin\theta_0\cos\varphi_0)\,\Delta H_Y - (\sin\theta_0)\,\Delta H_Z\right], \tag{A1}$$

$$\begin{aligned}\Delta\varphi = {} & \frac{\Delta H_X\sin\theta_0\sin\varphi_0}{F_1F_2}\left[H_A(2\cos^2\theta_0\cos^2\varphi_0 + \cos 2\theta_0\sin^2\varphi_0) - H_K\cos 2\theta_0 - \vec{H}\cdot\hat{m} - (H_X\sin\varphi_0 - H_Y\cos\varphi_0)\frac{\cos^2\theta_0\cos\varphi_0}{\sin\theta_0\sin\varphi_0}\right] \\ & + \frac{\Delta H_Y\sin\theta_0\cos\varphi_0}{F_1F_2}\left[H_A(2\cos^2\theta_0\sin^2\varphi_0 - \cos 2\theta_0\sin^2\varphi_0) + H_K\cos 2\theta_0 + \vec{H}\cdot\hat{m} - (H_X\sin\varphi_0 - H_Y\cos\varphi_0)\frac{\cos^2\theta_0\sin\varphi_0}{\sin\theta_0\cos\varphi_0}\right] \\ & + \frac{\Delta H_Z\sin\theta_0}{F_1F_2}\left[-\frac{1}{2}H_A\sin 2\theta_0\sin 2\varphi_0 + \cos\theta_0\,(H_X\sin\varphi_0 - H_Y\cos\varphi_0)\right].\end{aligned} \tag{A2}$$

F_1, F_2, and C are described after Eqs. (12) and (13). These expressions are valid for any equilibrium magnetization direction and are general for arbitrary values of each parameter (no approximation made). Equations (A1) and (A2) can be simplified if we make the following assumptions. First, if $|H_A| \ll |H\sin\theta_H|$, then Eq. (6) gives $\varphi_0 = \varphi_H$. Substituting this into Eqs. (A1) and (A2) gives

$$\Delta\theta = \frac{\cos\theta_0\,(\Delta H_X\cos\varphi_H + \Delta H_Y\sin\varphi_H) + \sin\theta_0\,[C\,(-\Delta H_X\sin\varphi_H + \Delta H_Y\cos\varphi_H) - \Delta H_Z]}{(H_K - H_A\sin^2\varphi_H)\cos 2\theta_0 + H\cos(\theta_H - \theta_0) - \frac{1}{2}CH_A\sin 2\theta_0\sin 2\varphi_H}, \tag{A3}$$

$$\begin{aligned}\Delta\varphi = {} & \frac{[(H_K - H_A\sin^2\varphi_H)\cos 2\theta_0 + H\cos(\theta_H - \theta_0)](-\Delta H_X\sin\varphi_H + \Delta H_Y\cos\varphi_H)}{\left[(H_K - H_A\sin^2\varphi_H)\cos 2\theta_0 + H\cos(\theta_H - \theta_0) - \frac{1}{2}CH_A\sin 2\theta_0\sin 2\varphi_H\right][-H_A\sin\theta_0\cos 2\varphi_H + H\sin\theta_H]} \\ & + \frac{H_A\sin 2\varphi_H[\cos^2\theta_0(\Delta H_X\cos\varphi_H + \Delta H_Y\sin\varphi_H) - \frac{1}{2}\sin 2\theta_0\Delta H_Z]}{\left[(H_K - H_A\sin^2\varphi_H)\cos 2\theta_0 + H\cos(\theta_H - \theta_0) - \frac{1}{2}CH_A\sin 2\theta_0\sin 2\varphi_H\right][-H_A\sin\theta_0\cos 2\varphi_H + H\sin\theta_H]},\end{aligned} \tag{A4}$$

where C [see after Eq. (13)] is now simplified as $C = \frac{H_A\cos\theta_0\sin 2\varphi_H}{-H_A\sin\theta_0\cos 2\varphi_H + H\sin\theta_H}$. We then consider cases when the in-plane component of the external field is directed along one of the Cartesian coordinate axes (along x or y axis), which allows one to drop terms with $\sin(2\varphi_H)$ and thus C becomes zero. Equations (A3) and (A4) then reduce to Eqs. (14) and (15).

2. Calculations of the Oersted field

The Oersted field is calculated using the following formula. We consider a conductive layer (gray slab in Fig. 8) with width w and thickness d. The center of the z axis is placed at the top surface of the slab; the y-axis (along the width direction) center is located at the center of the slab (see Fig. 8). The y and z components of the Oersted field, H_Y and H_Z, respectively, at coordinate (y, z) when current I is passed along the gray slab in Fig. 8 is

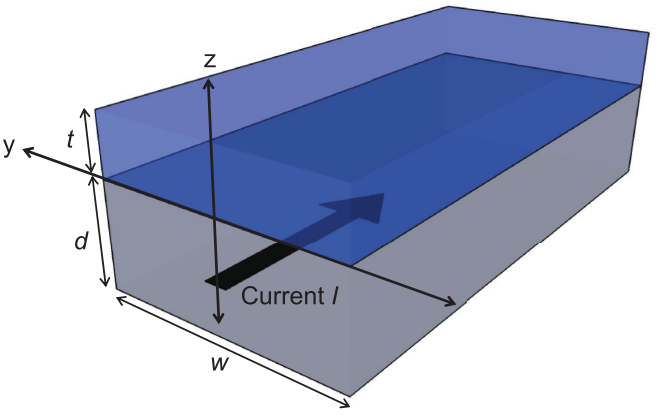

FIG. 8. (Color online) Schematic illustration of the setup used to calculate the Oersted field. Current is assumed to flow in the bottom layer (gray slab). The profile of the Oersted field is calculated in the upper layer (blue slab).

given [52] by (in Oersted)

$$
\begin{aligned}
H_Y(y,z) &= \frac{I}{wd}[U_Y^+(y,z) - D_Y^+(y,z) + U_Y^-(y,z) - D_Y^-(y,z)] \times 10^{-3},\\
U_Y^{\pm}(y,z) &= 2(z+d)\arctan\left[\frac{w/2 \pm y}{z+d}\right] + \left(\frac{w}{2} \pm y\right)\ln\left[\left(\frac{w}{2} \pm y\right)^2 + (z+d)^2\right],\\
D_Y^{\pm}(y,z) &= 2z\arctan\left[\frac{w/2 \pm y}{z}\right] + \left(\frac{w}{2} \pm y\right)\ln\left[\left(\frac{w}{2} \pm y\right)^2 + z^2\right],
\end{aligned}
\tag{A5}
$$

$$
\begin{aligned}
H_Z(y,z) &= \frac{I}{wd}[U_Z^+(y,z) - D_Z^+(y,z) - U_Z^-(y,z) + D_Z^-(y,z)] \times 10^{-3},\\
U_Z^{\pm}(y,z) &= 2\left(\frac{w}{2} \pm y\right)\arctan\left[\frac{z+d}{w/2 \pm y}\right] + (z+d)\ln\left[\left(\frac{w}{2} \pm y\right)^2 + (z+d)^2\right],\\
D_Z^{\pm}(y,z) &= 2\left(\frac{w}{2} \pm y\right)\arctan\left[\frac{z}{w/2 \pm y}\right] + z\ln\left[\left(\frac{w}{2} \pm y\right)^2 + z^2\right].
\end{aligned}
\tag{A6}
$$

To obtain H_Y in a magnetic layer (blue slab in Fig. 8) placed above the conductive slab, $H_Y(y, z)$ given by Eq. (A5) can be integrated along y from $-w/2$ to $w/2$ and along z from 0 to t (t is the thickness of the magnetic layer). We use $d = 3$nm for Pt|CoFeB|MgO, $d = 10$ nm for CuIr|CoFeB|MgO, and $w = 10$ μm for both structures.

[1] M. I. Dyakonov and V. I. Perel, Phys. Lett. A **35**, 459 (1971).
[2] J. E. Hirsch, Phys. Rev. Lett. **83**, 1834 (1999).
[3] S. F. Zhang, Phys. Rev. Lett. **85**, 393 (2000).
[4] Y. A. Bychkov and E. I. Rashba, J. Phys. C **17**, 6039 (1984).
[5] V. M. Edelstein, Solid State Commun. **73**, 233 (1990).
[6] J. C. Slonczewski, J. Magn. Magn. Mater. **159**, L1 (1996).
[7] L. Berger, Phys. Rev. B **54**, 9353 (1996).
[8] S. Zhang and Z. Li, Phys. Rev. Lett. **93**, 127204 (2004).
[9] A. Manchon and S. Zhang, Phys. Rev. B **78**, 212405 (2008).
[10] T. Fujita, M. B. A. Jalil, S. G. Tan, and S. Murakami, J. Appl. Phys. **110**, 121301 (2011).
[11] K. W. Kim, S. M. Seo, J. Ryu, K. J. Lee, and H. W. Lee, Phys. Rev. B **85**, 180404 (2012).
[12] X. Wang and A. Manchon, Phys. Rev. Lett. **108**, 117201 (2012).
[13] D. A. Pesin and A. H. MacDonald, Phys. Rev. B **86**, 014416 (2012).
[14] E. van der Bijl and R. A. Duine, Phys. Rev. B **86**, 094406 (2012).
[15] P. M. Haney, H. W. Lee, K. J. Lee, A. Manchon, and M. D. Stiles, Phys. Rev. B **87**, 174411 (2013).
[16] I. M. Miron, K. Garello, G. Gaudin, P. J. Zermatten, M. V. Costache, S. Auffret, S. Bandiera, B. Rodmacq, A. Schuhl, and P. Gambardella, Nature (London) **476**, 189 (2011).
[17] L. Liu, C.-F. Pai, Y. Li, H. W. Tseng, D. C. Ralph, and R. A. Buhrman, Science **336**, 555 (2012).
[18] I. M. Miron, T. Moore, H. Szambolics, L. D. Buda-Prejbeanu, S. Auffret, B. Rodmacq, S. Pizzini, J. Vogel, M. Bonfim, A. Schuhl, and G. Gaudin, Nat. Mater. **10**, 419 (2011).
[19] K.-S. Ryu, L. Thomas, S.-H. Yang, and S. Parkin, Nat. Nanotechnol. **8**, 527 (2013).
[20] U. H. Pi, K. W. Kim, J. Y. Bae, S. C. Lee, Y. J. Cho, K. S. Kim, and S. Seo, Appl. Phys. Lett. **97**, 162507 (2010).
[21] I. M. Miron, G. Gaudin, S. Auffret, B. Rodmacq, A. Schuhl, S. Pizzini, J. Vogel, and P. Gambardella, Nat. Mater. **9**, 230 (2010).
[22] T. Suzuki, S. Fukami, N. Ishiwata, M. Yamanouchi, S. Ikeda, N. Kasai, and H. Ohno, Appl. Phys. Lett. **98**, 142505 (2011).
[23] J. Kim, J. Sinha, M. Hayashi, M. Yamanouchi, S. Fukami, T. Suzuki, S. Mitani, and H. Ohno, Nat. Mater. **12**, 240 (2013).
[24] K. Garello, I. M. Miron, C. O. Avci, F. Freimuth, Y. Mokrousov, S. Blugel, S. Auffret, O. Boulle, G. Gaudin, and P. Gambardella, Nat. Nanotechnol. **8**, 587 (2013).
[25] S. Emori, U. Bauer, S.-M. Ahn, E. Martinez, and G. S. D. Beach, Nat. Mater. **12**, 611 (2013).
[26] X. Fan, J. Wu, Y. Chen, M. J. Jerry, H. Zhang, and J. Q. Xiao, Nat. Commun. **4**, 1799 (2013).
[27] M. Yamanouchi, L. Chen, J. Kim, M. Hayashi, H. Sato, S. Fukami, S. Ikeda, F. Matsukura, and H. Ohno, Appl. Phys. Lett. **102**, 212408 (2013).
[28] P. Balaz, J. Barnas, and J. P. Ansermet, J. Appl. Phys. **113**, 193905 (2013).
[29] T. R. McGuire and R. I. Potter, IEEE Trans. Magn. **11**, 1018 (1975).
[30] H. X. Tang, R. K. Kawakami, D. D. Awschalom, and M. L. Roukes, Phys. Rev. Lett. **90**, 107201 (2003).
[31] S. Zhang, P. M. Levy, and A. Fert, Phys. Rev. Lett. **88**, 236601 (2002).
[32] J. C. Slonczewski, J. Magn. Magn. Mater. **247**, 324 (2002).
[33] G. E. W. Bauer, Y. Tserkovnyak, D. Huertas-Hernando, and A. Brataas, Phys. Rev. B **67**, 094421 (2003).
[34] S. Urazhdin, R. Loloee, and W. P. Pratt, Phys. Rev. B **71**, 100401 (2005).
[35] C. Boone, J. A. Katine, J. R. Childress, J. Zhu, X. Cheng, and I. N. Krivorotov, Phys. Rev. B **79**, 140404 (2009).
[36] J. Z. Sun, Phys. Rev. B **62**, 570 (2000).
[37] M. D. Stiles and J. Miltat, in *Spin Dynamics in Confined Magnetic Structures Iii* (Springer-Verlag Berlin, Berlin, 2006), Vol. 101, pp. 225.
[38] L. Q. Liu, O. J. Lee, T. J. Gudmundsen, D. C. Ralph, and R. A. Buhrman, Phys. Rev. Lett. **109**, 096602 (2012).
[39] O. Mosendz, J. E. Pearson, F. Y. Fradin, G. E. W. Bauer, S. D. Bader, and A. Hoffmann, Phys. Rev. Lett. **104**, 046601 (2010).

[40] M. Morota, Y. Niimi, K. Ohnishi, D. H. Wei, T. Tanaka, H. Kontani, T. Kimura, and Y. Otani, Phys. Rev. B **83**, 174405 (2011).
[41] L. Liu, R. A. Buhrman and D. C. Ralph, cond-mat., 1111.3702.
[42] Y. Niimi, M. Morota, D. H. Wei, C. Deranlot, M. Basletic, A. Hamzic, A. Fert, and Y. Otani, Phys. Rev. Lett. **106**, 126601 (2011).
[43] S. Ikeda, K. Miura, H. Yamamoto, K. Mizunuma, H. D. Gan, M. Endo, S. Kanai, J. Hayakawa, F. Matsukura, and H. Ohno, Nat. Mater. **9**, 721 (2010).
[44] J. C. Sankey, Y.-t. Cui, J. Z. Sun, J. C. Slonczewski, R. A. Buhrman, and D. C. Ralph, Nat. Phys. **4**, 67 (2008).
[45] H. Kubota, A. Fukushima, K. Yakushiji, T. Nagahama, S. Yuasa, K. Ando, H. Maehara, Y. Nagamine, K. Tsunekawa, D. D. Djayaprawira, N. Watanabe, and Y. Suzuki, Nat. Phys. **4**, 37 (2008).
[46] S. C. Oh, S. Y. Park, A. Manchon, M. Chshiev, J. H. Han, H. W. Lee, J. E. Lee, K. T. Nam, Y. Jo, Y. C. Kong, B. Dieny, and K. J. Lee, Nat. Phys. **5**, 898 (2009).
[47] S. Petit, C. Baraduc, C. Thirion, U. Ebels, Y. Liu, M. Li, P. Wang, and B. Dieny, Phys. Rev. Lett. **98**, 077203 (2007).
[48] Z. Li, S. Zhang, Z. Diao, Y. Ding, X. Tang, D. M. Apalkov, Z. Yang, K. Kawabata, and Y. Huai, Phys. Rev. Lett. **100**, 246602 (2008).
[49] T. Devolder, J. V. Kim, C. Chappert, J. Hayakawa, K. Ito, H. Takahashi, S. Ikeda, and H. Ohno, J. Appl. Phys. **105**, 113924 (2009).
[50] M. D. Stiles and A. Zangwill, Phys. Rev. B **66**, 014407 (2002).
[51] D. C. Ralph and M. D. Stiles, J. Magn. Magn. Mater. **320**, 1190 (2008).
[52] T. J. Silva, C. S. Lee, T. M. Crawford, and C. T. Rogers, J. Appl. Phys. **85**, 7849 (1999).